Disorder Induced Structural Complexity in the Barlowite Family of $S = \frac{1}{2}$ Kagomé Magnets

Katherine Tustain,[†] Emma E. McCabe,[‡] Angel M Arevalo-Lopez,[¶] Alexandra S. Gibbs,[§,‖] Stephen P. Thompson,[⊥] Claire A. Murray,[⊥] Clemens Ritter,[#] and Lucy Clark[*,@,†]

†*Department of Chemistry and Materials Innovation Factory, University of Liverpool, 51 Oxford Street, Liverpool L7 3NY, UK*

‡*Department of Physics, Durham University, South Road, Durham DH1 3LE, UK*

¶*Unité de Catalyse et Chimie du Solide, University of Lille, F-59000, Lille, France*

§*ISIS Neutron and Muon Source, Rutherford Appleton Laboratory, Didcot, OX11 0QX, UK*

‖*School of Chemistry, University of St Andrews, North Haugh, St Andrews, KY16 9ST, UK*

⊥*Diamond Light Source, Harwell Science and Innovation Campus, Didcot, OX11 0QX, UK*

#*Institut Laue-Langevin, 71 Avenue des Martyrs, F-38042, Grenoble, France*

@*School of Chemistry, University of Birmingham, Edgbaston, Birmingham B15 2TT, UK*

E-mail: l.m.clark@bham.ac.uk

Abstract

We present a comprehensive structural and magnetic characterisation of the barlowite family of $S = \frac{1}{2}$ kagomé magnets, $Cu_4(OH)_6FX$ where X = Cl, Br or I. Through high-resolution synchrotron X-ray and neutron powder diffraction measurements, we reveal two sources of structural complexity within this family of materials, namely compositional disorder of the halide species that occupy sites in between the kagomé layers, as well as positional disorder of the interlayer Cu^{2+} ions that persists well into

the *Pnma* structural ground state. We demonstrate that understanding these inherent structural disorders is key, as they correlate with the degree of partial order in the magnetic ground states of these quantum frustrated magnets.

Introduction

The discovery of naturally occurring mineral materials has for many decades provided a rich source of inspiration for the synthesis of inorganic crystalline solids, thus allowing for their ensuing materials properties to be explored[1]. This is especially so in the field of quantum materials, whereby the structural arrangement of metal ion centres in mineral systems and their corresponding interactions can give rise to fascinating and complex electronic and magnetic phenomena[2]. Often, this complexity arises from the frustration of the magnetic exchange interactions stemming from the underlying crystal structure. In the context of highly frustrated magnetism, one of the most long-sought models is that of the kagomé antiferromagnet, a two-dimensional array of corner-sharing equilateral triangles of antiferromagnetically coupled magnetic moments[3]. In the quantum ($S = \frac{1}{2}$) limit of this model, a variety of novel quantum states of matter—including quantum spin liquid (QSL) states[4]—have been predicted to emerge due to the combination of low magnetic dimensionality, competing magnetic exchange interactions and quantum fluctuations. The drive to realise, understand and exploit such quantum states of matter[5] means that synthetic analogues of mineral systems that contain kagomé networks of magnetic metal ions remain firmly in the spotlight[6–9].

In this regard, the atacamite family of minerals is a significant class of materials that offers a rich variety of structural and magnetic behaviours. There are three polymorphs within the atacamite family with the general formula $Cu_4(OH)_6Cl_2$: atacamite, botallackite and clinoatacamite[10]. Botallackite has a layered monoclinic structure in which Cu^{2+} ions form edge-sharing triangles, rather than a corner-sharing kagomé array. Atacamite and clinoatacamite, on the other hand, have orthorhombic and monoclinic structures, respectively, in

which distorted kagomé layers are separated by interlayer Cu^{2+} and Cl^{-} ions. However, due to the presence of magnetic exchange interactions within and between the kagomé layers, both of these systems are more appropriately described in terms of a three-dimensional pyrochlore model, rather than a two-dimensional kagomé one[11–13]. Helpfully, the clinoatacamite structure is stable to the replacement of its Cu^{2+} ions by isovalent diamagnetic species such as Zn^{2+}, and this substitution occurs predominantly at the interlayer site. Such a substitution alters the structure of the parent compound and reduces the interlayer magnetic exchange. In the case of Zn^{2+} substitution, the Zn-paratacamite series, $Zn_xCu_{4-x}(OH)_6Cl_2$, is formed, which has trigonal $R\bar{3}m$ symmetry for $x > 0.33$[14]. Compositions of this symmetry contain undistorted kagomé layers of Cu^{2+} separated by Cu^{2+}/Zn^{2+} and Cl^{-}, the latter being covalently bonded to Cu^{2+} ions in the layer above and hydrogen bonded to hydroxide groups in the layer below, leading to staggered stacking of the kagomé planes along the c axis. The $x = 1$ end-member of the Zn-paratacamite series, $ZnCu_3(OH)_6Cl_2$, is the mineral herbertsmithite which, in theory, should contain magnetically decoupled and undistorted $S = \frac{1}{2}$ kagomé layers. These structural features mean that—despite significant antiferrromagnetic exchange interactions between the Cu^{2+} ions within the kagomé planes—herbertsmithite lacks long-range magnetic order in its ground state, making it the first possible material realisation of a QSL on a kagomé network. However, herbertsmithite is known to suffer from Cu^{2+}/Zn^{2+} site occupancy disorder[15], which has made the characterisation of its magnetic ground state challenging[7,8,16,17]. Such structural complexities within these mineral systems thus provide the motivation for the discovery of alternative materials which may more clearly represent the $S = \frac{1}{2}$ kagomé antiferromagnet.

In recent years, the mineral barlowite, $Cu_4(OH)_6FBr$, has been hailed as a promising new material in this regard[18]. Formed from kagomé layers of Cu^{2+} ions separated by a mixture of Cu^{2+} and halide ions, F^{-} and Br^{-}, it is well established that barlowite orders antiferromagnetically below $T_N = 15$ K[17,19–25] with a magnetic structure determined by neutron

diffraction[26]. Density-functional theory (DFT) calculations indicate that—akin to the phenomena observed in the Zn-paratacamite series—replacement of the interlayer Cu^{2+} ions in barlowite with Zn^{2+} could decouple the kagomé layers[27], but with significantly increased site selectivity[28]. The order of magnitude reduction in Zn^{2+}/Cu^{2+} site occupancy disorder predicted for Zn-barlowite compared with herbertsmithite is thought to stem from the differences in their crystal structures. In barlowite, the presence of a mixture of halide species leads to eclipsed stacking of adjacent kagomé layers, which in turn affects the local symmetry at the interlayer Cu^{2+} site. DFT studies thus provide compelling impetus to explore barlowite as a new route towards the QSL that may provide much needed insight into the role of disorder in the ground state selection of the $S = \frac{1}{2}$ kagomé antiferromagnet through careful comparison to herbertsmithite. Indeed, experimental investigations of the Zn-barlowite series have since pointed to the formation of a QSL phase at low-temperatures.[29]

Despite this promise, however, barlowite remains the subject of intense debate in the literature, with several conflicting reports of its crystal structure, all of which are characterised by varying degrees of disorder on the interlayer Cu^{2+} site as represented in Fig. 1. In the widely reported room-temperature structure, which is described by a hexgonal $P6_3/mmc$ model, the interlayer Cu^{2+} cations are disordered over three equivalent sites[18,19,21,24,25,30], and the ordering of this site occupancy upon cooling leads to a symmetry lowering of the average crystal structure. There are two orthorhombic models that have been proposed to describe the low-temperature structure emerging from this order-disorder transition, $Pnma$[21,26] and $Cmcm$[22]. In both structures, the interlayer Cu^{2+} ions order onto one site, but the structures differ in the ordering schemes at the interlayer site. More recently, a third low-temperature structure of barlowite has been reported with hexagonal $P6_3/m$ symmetry, which appears to be favoured under certain synthetic conditions[30]. A key difference in the synthetic routes to samples of barlowite is the reagents used in the hyrdrothermal preparations. Samples reported in the $Cmcm$ space group are prepared from $CuCO_3{\cdot}Cu(OH)_2$, NH_4F and HBr[22],

where those reported in $P6_3/m$ are prepared from $CuBr_2$ and LiF[24]. In this low-temperature hexagonal structure, the kagomé layers are formed from alternating equilateral and scalene triangles, and it follows that the interlayer Cu^{2+} sites contain a mixture of ordered and disordered occupancies. One study ascribes the structural transition in barlowite to a dynamic-to-static Jahn-Teller effect that can vary between different samples owing to the presence of defects[25]. Intriguingly, the magnetic properties of barlowite appear to be highly dependent on the precise crystal structure adopted at low temperature, indicating that each reported structural model is characterised by its own magnetic ground state[30]. As a consequence, a definitive understanding of the factors that drive this structural distortion and govern the structural ground state of barlowite and its analogues is imperative.

Indeed, the structural complexity presented in barlowite raises the question as to whether one can systematically tune its structure in order to rationalise the structure-property relationships at play. Inspection of the crystal structure of barlowite yields one particularly promising route to achieve this goal, which is to apply chemical pressure through the substitution of the halide ions in between the kagomé layers as depicted in Fig. 2. In the room-temperature $P6_3/mmc$ structural model of barlowite, bromide ions sit on the $2c$ Wyckoff position, bonding to three Cu^{2+} ions above and three below to complete the octahedral coordination of the Cu^{2+} ions in the kagomé planes. Meanwhile, the fluoride ions hydrogen bond to six surrounding hydroxide groups in the $2b$ position. Given the large void in which the bromide ions sit at the $2c$ site—along with the high electronegativity of the fluoride ions in the $2b$ position—substitution of Br^- for Cl^- or I^- at the $2c$ site is the natural choice to apply both negative and positive chemical pressure to the structure.

Thus, to address the complexities surrounding the structure and properties of barlowite, here we present a comprehensive study of this material, $Cu_4(OH)_6FBr$, its chloride analogue claringbullite, $Cu_4(OH)_6FCl$[25,31,32], and a novel synthetic iodide analogue, $Cu_4(OH)_6FI$. We

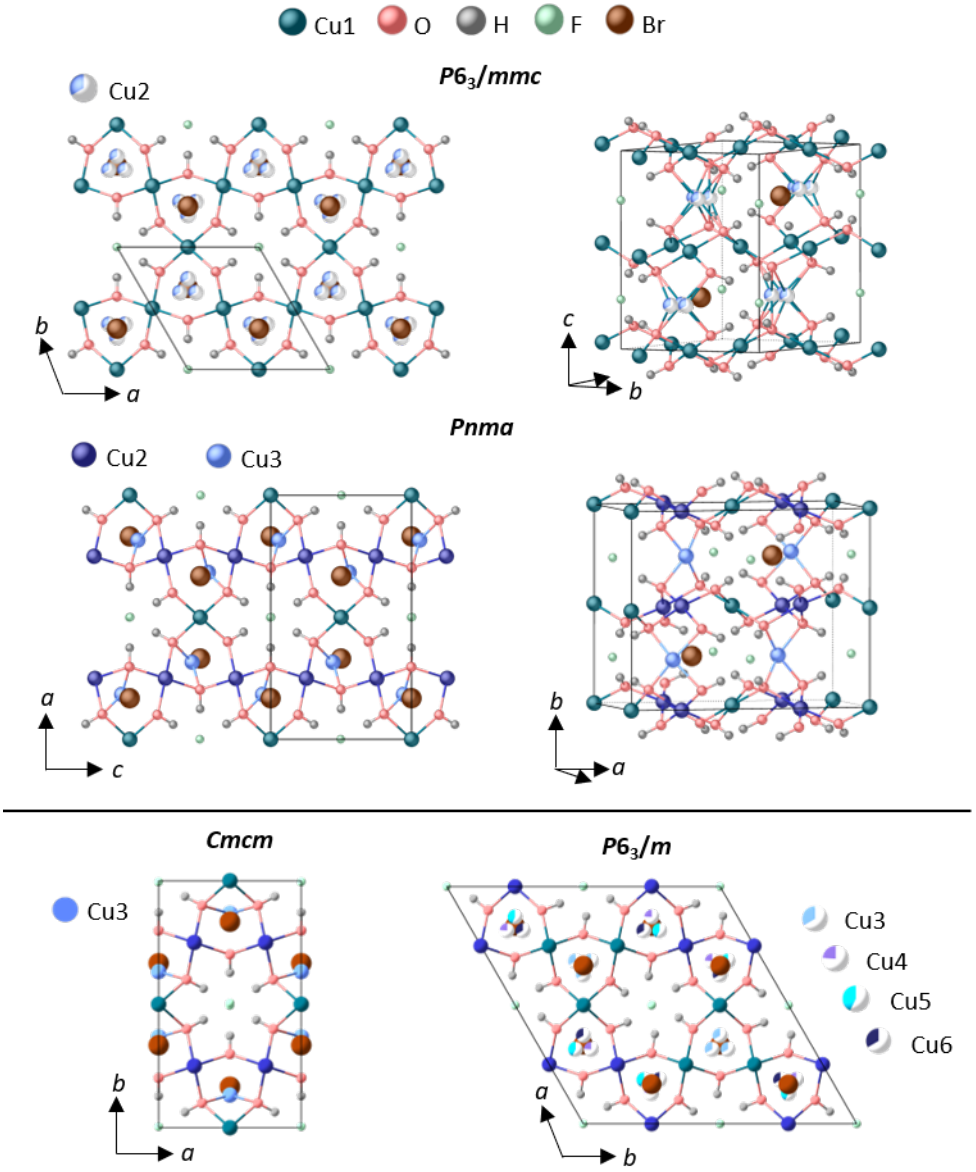

Figure 1: **Conflicting structural models of barlowite**. At room temperature, the structure of barlowite ($Cu_4(OH)_6FBr$) is widely reported in the $P6_3/mmc$ model (top), which contains Cu^{2+} kagomé layers in the *ab* plane and an additional Cu^{2+} site between the layers that is disordered. Upon cooling, lower symmetry structures are reported to emerge. In the *Pnma* structure (middle), the kagomé layers are formed from two Cu^{2+} sites, and the occupation at the interlayer site is considered to be fully ordered.[21,26] The alternatively proposed structural models of barlowite (bottom) are *Cmcm*,[22] which differs in its ordering scheme to *Pnma*, and $P6_3/m$,[30] which retains site occupancy disorder at the interlayer Cu^{2+} sites. Partially shaded spheres indicate partial site occupancy due to site occupancy disorder.

combine high-resolution synchrotron X-ray and neutron powder diffraction data for barlowite and its halide analogues to elucidate the temperature-dependent structural behaviour observed in these phases, revealing both positional and compositional disorder within their ground state structures. Through magnetometry, heat capacity and high-flux powder neutron diffraction measurements, we correlate this structural disorder to the complex behaviour displayed in the magnetic ground state of this family.

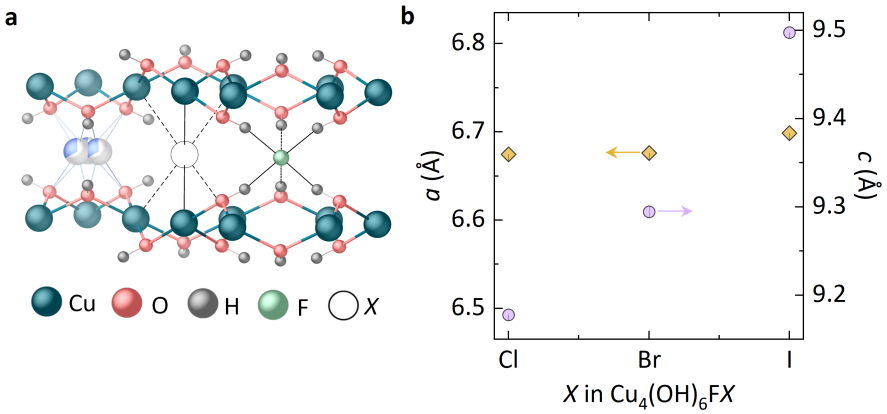

Figure 2: **Tuning the structure and properties of barlowite.** (a) In between the kagomé layers of barlowite are a disordered interplane Cu^{2+} site (represented by partially shaded spheres) and a fluoride site at the 2*b* position, created by the surrounding hydroxide groups. In barlowite, the second halide site, X, at the 2*c* position is occupied by bromide ions, but substitution at this site for chloride or iodide can tune the structure by applying negative or positive chemical pressure. (b) The refined room-temperature lattice parameters of the $P6_3/mmc$ model applied across the $Cu_4(OH)_6FX$ reveals the expansion of the c axis upon this substitution. Error bars representing the standard error of the fitted lattice parameters are smaller than the data points shown.

Experimental Section

Hydrothermal synthesis

Polycrystalline samples of deuterated $Cu_4(OD)_6FX$ (X = Br, Cl, I) were synthesised via a hydrothermal method. Barlowite ($Cu_4(OD)_6FBr$, referred to hereafter as **FBr**) was produced by combining 4 mmol $CuCO_3{\cdot}Cu(OH)_2$ (Alfa Aesar, Cu 55%), 12 mmol NH_4F (Alfa Aesar, 98%) and 8 mmol $CuBr_2$ (Sigma Aldrich, 99%) with 20 mL D_2O (Sigma Aldrich, 99.9% D) in a 50 mL PTFE-lined stainless steel autoclave. The sealed autoclave was heated to 200 °C at a rate of 10 °C/min and held at temperature for 72 hours. After heating, the autoclave was cooled to room temperature at 5 °C/min and the polycrystalline sample was collected by filtration, washed with D_2O and dried in air. Claringbullite ($Cu_4(OD)_6FCl$, referred to hereafter as **FCl**) was synthesised by combining 2 mmol $CuCO_3{\cdot}Cu(OH)_2$ (Alfa Aesar, Cu 55%), 4 mmol NH_4F (Alfa Aesar, 98%) and 2 mmol $CuCl_2$ (Acros Organics, 99%) with 10 mL D_2O in a 23 mL PTFE-lined stainless steel autoclave. The sealed autoclave was heated to 200 °C at a rate of 10 °C/min and held at temperature for 48 hours. After heating, the autoclave was cooled to room temperature at 5 °C/min and the polycrystalline sample was collected by filtration, washed with D_2O and dried in air. Compared with the synthesis of FBr, FCl required an excess of NH_4F to avoid the formation of polymorphs of clinoatacamite ($Cu_4(OH)_6Cl_2$), which form when an excess of Cl^- ions is present in the reaction mixture. Finally, the iodide analogue ($Cu_4(OD)_6FI$, referred to hereafter as **FI**) was synthesised by combining 2 mmol $CuCO_3{\cdot}Cu(OH)_2$ (Alfa Aesar, Cu 55%), 2 mmol NH_4F (Alfa Aesar, 98%) and 0.2 mL HI (Sigma Aldrich, 58%) with 10 mL D_2O in a 23 mL PTFE-lined stainless steel autoclave. The sealed autoclave was heated to 140 °C at a rate of 10 °C/min and held at temperature for 72 hours. After heating, the autoclave was cooled to room temperature at 5 °C/min. This method resulted in a minor CuI impurity phase, which was removed by stirring the sample in a dilute aqueous solution of ammonium hydroxide. Note that heating to temperatures above 150 °C in the synthesis of FI failed to produce the desired product,

leading to CuO and CuI instead. Each synthesis was repeated several times for sample scale up, and the resulting samples were combined and ground thoroughly to produce sample volumes adequate for powder neutron diffraction measurements. Batches of the same samples were measured for all of the diffraction experiments included in this work. Magnetometry and heat capacity measurements were performed on protonated samples synthesised via the same routes reported here but with H_2O rather than D_2O as a solvent.

Structural characterisation

High-resolution powder x-ray diffraction (PXRD) data were collected on the I11 beamline of the Diamond Light Source. Samples of FCl, FBr and FI were packed into borosilicate glass capillaries and attached to a brass holder. Each sample was cooled using a Cryostream, and data were collected with an X-ray wavelength $\lambda = 0.826582$ Å on the MAC detector at 90 K and 300 K. For FBr, additional MAC measurements were conducted between 90 – 300 K in 20 K steps. For FCl and FI, additional data were collected between 90 – 300 K in 2 K steps on the PSD detector. High-resolution powder neutron diffraction (PND) data were collected on the HRPD instrument at the ISIS Neutron and Muon Source. Each sample (3.2 g FCl, 4.2 g FBr and 2.5 g FI) was packed into a aluminium alloy flat-plate holder with steel-framed vanadium windows. Data were collected for each sample at 1.5 K and 300 K.

Magnetic characterisation

Temperature-dependent magnetic susceptibility data were collected on a Quantum Design MPMS3 SQUID magnetometer in DC measurement mode. 40 mg samples of FCl, FBr and FI were packed into gelatin capsules and loaded into plastic straw samples holders. Data were collected in an applied field of 1 T between 2 – 300 K. Heat capacity data were collected on pressed powder pellets of FCl (9.5 mg), FBr (26.4 mg) and FI (12.4 mg) in a Quantum Design PPMS Dynacool in zero field between 2 – 300 K. An addenda for each was measured and subtracted. Two data points per temperature were collected and averaged.

High-flux PND data were collected on the D20 instrument at the Institut Laue-Langevin. Each sample (3.1 g FCl, 4.2 g FBr and 1.2 g FI) was packed into a cylindrical vanadium can of diameter 9 mm (FCl, FBr) or 6 mm (FI) and data were collected with a neutron wavelength $\lambda = 2.4188$ Å and a monochromator take-off angle 42°. Data were collected at 1.5 K, 10 K and 25 K for FCl, 1.5 K and 20 K for FBr, and 1.5 K and 25 K for FI.

Data analysis

Rietveld refinement of structural models to high-resolution powder diffraction data were performed using the GSAS software suite. Symmetry-allowed magnetic models were generated using the MAXMAGN application on the Bilbao Crystallographic Server. Magnetic structure refinement was performed against high-flux PND difference data sets containing only magnetic scattering in the FULLPROF software package. Curie-Weiss fitting of temperature-dependent inverse molar magnetic susceptibility, $\chi_m^{-1} = T - \theta_{\mathsf{CW}}/C$, was perfomed in the OriginPro software package to extract Weiss temperatures, θ_{CW}, and Curie constants, $C = N_{\mathsf{A}}\mu_0{\mu_{\mathsf{eff}}}^2/3k_{\mathsf{B}}$, for each sample. OriginPro was also used to fit and subtract an estimate of the lattice contribution to the total heat capacity of each sample, $C_{\mathsf{lat}} = \alpha T^2 + \beta T^3$, yielding an estimate of the magnetic heat capacity, C_{mag}, for each. The magnetic entropy release, S_{mag}, through the magnetic transitions of each sample was calculated by integrating C_{mag} over 2 – 25 K.

Results & Discussion

Compositional disorder compounding structural complexity

As detailed above, the widely accepted structural model for barlowite at room temperature is that described by the hexagonal space group $P6_3/mmc$ shown in Fig. 1. Initial analysis of the high-resolution neutron and X-ray powder diffraction data collected at 300 K across the $Cu_4(OH)_6FX$ series reveals that the diffraction patterns of each halide analogue can be in-

dexed with the same $P6_3/mmc$ space group. Fitting this structural model to the diffraction data across the series, we observe that the hexagonal unit cell is predominantly expanded along the c axis as the size of the halide occupying the $2c$ site increases from 1.81 Å for Cl^- to 2.2 Å for I^-, with only a small increase in the ab plane as shown in Fig. 2b. However, Rietveld refinement of this model to data collected at 300 K for FI reveals a particularly poor fit, especially to the Bragg peaks of $hk4\mathsf{n}$-type reflections. An example of this effect—observed in both the high-resolution PXRD and PND data—is shown in Fig. 3. Inspection of $hk4\mathsf{n}$-type Bragg peaks of the FI system clearly reveals an asymmetric peak profile that tails towards high Q.

An asymmetric peak profile of this kind often indicates a range of compositions of the main phase of a polycrystalline sample[33]. In this family of layered materials, while there is little variation of the in-plane a unit cell parameter with choice of halide X, the c parameter is sensitive to the halide size and distribution in between the kagomé layers as shown in Fig. 2b. Thus, a likely explanation for the asymmetric shape of hkl peaks with high l indices for FI samples is a variation in the F/I site occupancy ratio, giving rise to a distribution of values for the c parameter, ranging from the majority phase fraction with the largest c parameter to increasingly smaller amounts of phases with lower c parameters due to higher F^- content. Close inspection of laboratory powder X-ray diffraction data of single batches of FI reveal the same pattern of asymmetric peak shapes, indicating that this feature in our data does not simply stem from the combination of multiple synthesis batches. Thus, to test our hypothesis of compositional variance, a Rietveld refinement of multiple $P6_3/mmc$ phases with differing c axis parameters was performed simultaneously to the 300 K X-ray and neutron data of FI. This follows a similar approach to that of David *et al.*[33], with the combined refinements using X-ray and neutron data allowing good contrast between F^- and I^-, giving confidence in the refined halide site occupancy ratios. Several measures were taken to constrain this multi-phase refinement. First, the a and b unit cell parameters were fixed to

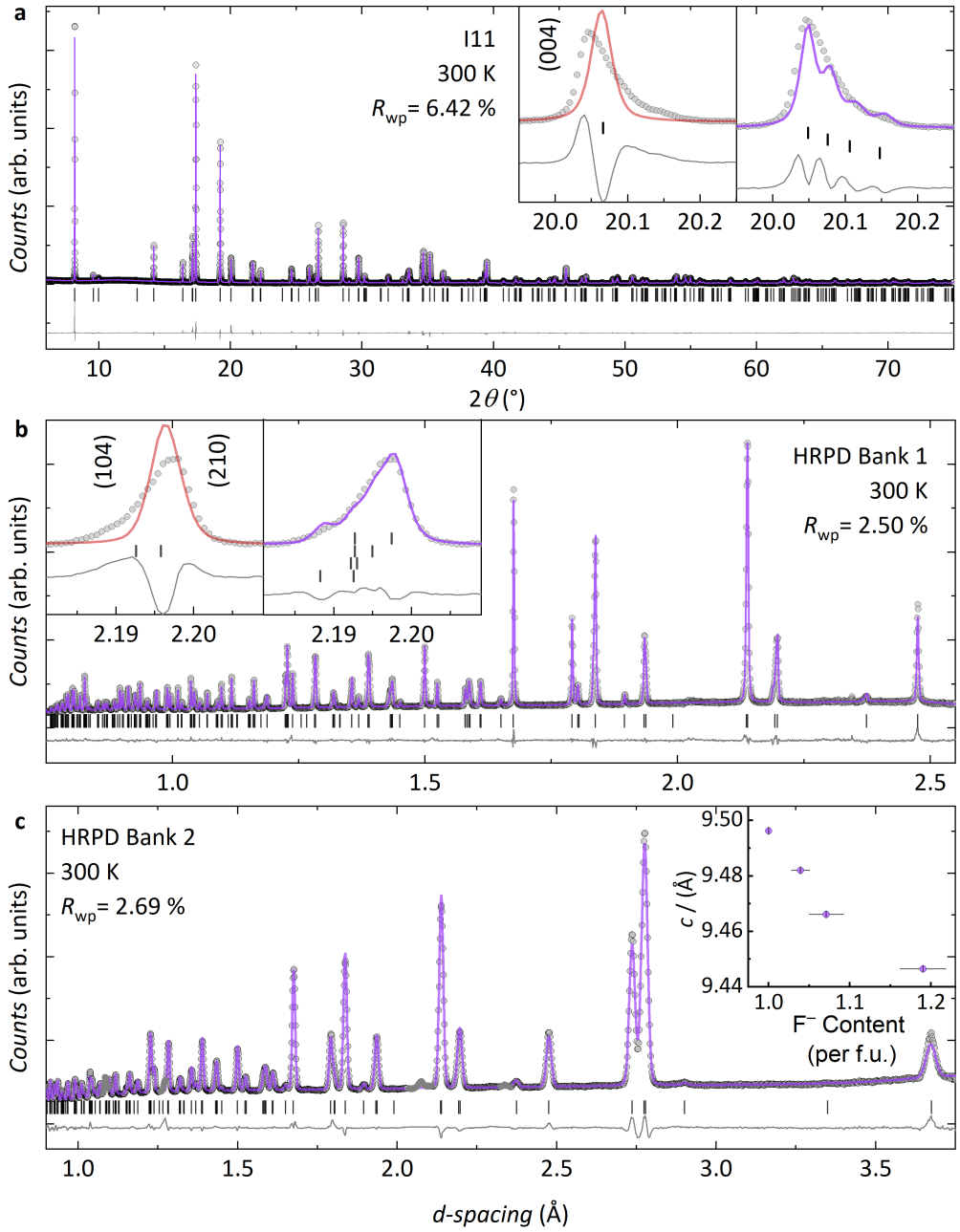

Figure 3: **Modelling compositional disorder in $Cu_4(OH)_6FX$.** Rietveld refinement of four $P6_3/mmc$ models to powder diffraction data collected for FI at 300 K on (a) I11 and HRPD (b) Bank 1 and (c) Bank 2. Tick marks for just one phase are included in the main panels for clarity. The insets in (a) and (b) show the most prominent asymmetric $hk4\mathsf{n}$ reflections in the data, with a comparison of single-phase and four-phase models. In (c) the light grey regions in the data due to steel in the sample holder are excluded from the fit, and the inset shows refined c axis parameters against the refined F^- content.

be equal across the phases, so that only the c parameter was allowed to vary for each phase. Second, the atom positions and isotropic atomic displacement parameters, U_{iso}, were also constrained across the phases, as well as peak profile parameters. Finally, for each phase, the site occupancy ratio of F/I was refined across the two halide sites in the $P6_3/mmc$ model, with the constraint that each site must remain fully occupied. A high level of anion order was found for the phase closest to ideal stoichiometry, with the $2b$ site fully occupied by F^- and the $2c$ site almost fully occupied by I^-.

A total of four phases could be modelled effectively in this way. The refined structural model is given in Table 1 along with the refined phase fractions and F/I occupancies of each of the four phases. The results of this analysis indicate that there is a range of fluoride-rich phases present within FI, in which excess fluoride ions occupy the $2c$ site. The inset to Fig. 3c demonstrates that the refined c axis parameter systematically decreases with increasing fluoride content within a given phase. This analysis does not suggest since the presence of four distinct phases within the FI sample, since further phases at intermediate compositions can be included within the refinements but with increasingly insignificant improvements in the quality of the fit. Instead, it offers an approximation for a phase continuum that appears to be driven by compositional disorder arising between the kagomé layers that further compounds the structural complexity within this family of materials. The multi-phase fitting allows for a marked improvement to the quality of the Rietveld fit, with a total $R_{\mathsf{wp}} = 3.40$ % compared to $R_{\mathsf{wp}} = 6.16$ % for the single-phase refinement. However, by itself, it cannot explain whether the observed variation in c-axis parameters is due to compositional disorder between the kagomé layers of individual crystallites—which could be considered a type of stacking fault—or a compositional variance between different crystallites.

Nevertheless, the discovery of compositional disorder in FI led us to question whether the same phenomenon might occur within FCl and FBr. Indeed, close inspection of the high-

Table 1: Structural parameters obtained from the Rietveld refinement of the $P6_3/mmc$ model of FI to I11 and HRPD data collected at 300 K. The simultaneous analysis of X-ray and neutron data sets allows for the refinement of both the deuterium fractional coordinates–not possible through X-ray diffraction alone—and the F/I site occupancies, for which X-rays are required as neutron scattering contrast is poor. The bottom table shows the phase fractions, c axis parameters and F/I occupancies for each of the four refined $P6_3/mmc$ phases. The total statistical parameters for the combined fits are $R_{\mathsf{wp}} = 3.40$ % and $\chi^2 = 5.916$.

Atom	Site	x	y	z	Occupancy	U_{iso} (Å^2)
Cu1	$6g$	0.5	0	0	1	0.0099(1)
Cu2	$6h$	0.6304(1)	0.2609(2)	0.25	$\frac{1}{3}$	0.0086(4)
O1	$12k$	0.20321(7)	0.79679(7)	0.90863(7)	1	0.0095(2)
D1	$12k$	0.12548(7)	0.87452(7)	0.86814(8)	1	0.0247(2)
F1	$2b$	0	0	0.75	1	0.0174(4)
I1	$2b$	0	0	0.75	0	0.0174(4)
F2	$2c$	0.6667	0.3333	0.75	*	0.0129(1)
I2	$2c$	0.6667	0.3333	0.75	*	0.0129(1)

	Phase number			
*	1	2	3	4
Phase fraction (%)	46.3(1)	27.2(2)	16.1(2)	10.4(2)
c (Å)	9.49742(4)	9.48472(9)	9.4706(2)	9.4511(1)
F2 occupancy	0	0.04(1)	0.08(2)	0.19(3)
I2 occupancy	1	0.96(1)	0.92(2)	0.82(3)

resolution PXRD and PND data of both systems reveals a subtle asymmetry of the $hk4\mathsf{n}$-type reflections. As such, co-fitting the X-ray and neutron data collected at 300 K for each sample was conducted using multiple $P6_3/mmc$ phases, again constraining the model so that only the c-axis parameters and F/X ratios were allowed to vary across the phases. The Rietveld refinements of two $P6_3/mmc$ phases are shown in the Supporting Information along with the corresponding tabulated refinement results. The inclusion of a second phase improves the $hk4\mathsf{n}$ peak fitting for both FCl and FBr, which is reflected in the total R_{wp} values decreasing from 4.21 % to 3.63 % for FCl and 4.05 % to 3.54 % for FBr. Refinement of the F/X site occupancies for FBr reveals a $\sim 5\%$ fluoride occupancy on the bromide site in the fluoride-rich phase, leading to a contraction of the c axis parameter akin to the compositional disorder

observed in FI. In FCl, on the other hand, $\sim$ 7 % chloride anions were found to occupy the fluoride site of the second phase. There are two possible explanations for this observed behaviour. First, perhaps the poorer X-ray contrast between F/Cl compared with F/Br and F/I makes refining the occupancies more challenging for FCl. Alternatively, perhaps the more comparable ionic radii of F^- and Cl^- means that chloride can indeed occupy the fluoride ion site in FCl. Note that employing more than two $P6_3/mmc$ phases in the analysis of FCl and FBr led to an unstable refinement in both cases, implying that the compositional disorder is more pronounced in FI.

Interestingly, this is not the first time that the compositional distribution of anions within the $Cu_4(OH)_6FX$ family has been called into question. In the original mineralogical study of claringbullite (FCl), the chemical formula was reported as $Cu_4(OH)_7Cl{\cdot}H_2O$.[31] This was subsequently revised to $Cu_4(OH)_6Cl[Cl_{0.29}(OH)_{0.71}]$, meaning that the 2*b* site was thought to be occupied by a combination of Cl^- and OH^- ions rather than F^-, and that a solid solution of $Cu_4(OH)_{6+x}Cl_{2-x}$ could exist.[32] Following this, exploration into the methods required to synthetically prepare FCl determined that a fluoride source is necessary, and from the structural characterisation of synthetic samples, it was concluded that the 2*b* site was solely occupied by F^- based on refinement *R*-factors.[34] Most recently, however, a revisited crystallographic study of mineral samples of FCl determined a Cl:F:OH ratio of 0.98:1.12:5.90.[35] Therefore, it is highly plausible that there exists a range of compositions with the formula $Cu_4(OH)_xF_yCl_z$ where $x + y + z = 8$ for synthetic samples too, with the exact range of compositions accessed governed by the synthetic conditions. Based on our current analysis, we cannot rule out the possibility of hydroxide-halide site disorder within our samples, but note that modelling such disorder is extremely challenging given the lack of neutron and X-ray scattering contrast for O and F. However, across the $Cu_4(OH)_6FX$ series, the halide site selectivity driving the F/X disorder that we do observe is likely influenced by both the relative ionic radii and electronegativity of the F/X species. Whilst the comparably large ra-

dius and low electronegativity of the bromide ion mean that it is unlikely to occupy the small hydrogen-rich pocket within which the fluoride ions lie, it is plausible that excess fluoride could occupy the large space occupied by the bromide ions in the case of FBr. Meanwhile in FI, the apparently more pronounced compositional disorder may stem from the larger ionic radius of I^-, imposing strain within the crystal structure and causing fluoride rich phases to form more favourably than the stoichiometric FI phase.

Positional disorder driving the structural transition

Having established the room-temperature structure of the $Cu_4(OH)_6FX$ series, we next explore the temperature-dependent behaviour to elucidate its structural ground state. In our previous investigation of FBr, we established that below $\sim$ 250 K, samples of FBr prepared via the synthesis method described in the Experimental Section adopt the orthorhombic *Pnma* structure depicted in Fig. 1. Fig. 4 shows high-resolution PXRD data collected on the I11 instrument for each member of the series upon cooling. Here, one can clearly observe the development of additional Bragg peaks at approximately 266 K, 220 K and 274 K for FCl, FBr and FI, respectively, which can be indexed with the orthorhombic *Pnma* space group of the low-temperature structure determined previously for FBr. Fig. 4 also shows the temperature evolution of the intensity of the most prominent orthorhombic distortion peak (102), extracted by fitting a pseudo-Voigt function to the peak at every temperature point measured and plotted relative to the intensity of the most intense (110) at 90 K for each $Cu_4(OH)_6FX$ analogue. These data show that the hexagonal to orthorhombic structural transition occurs over a wide range of temperatures, particularly for FCl and FBr, where the (102) peak intensity does not plateau within the temperature window accessible during the I11 experiment. For FBr, the orthorhombic peak intensity is so weak that the MAC detector—which requires longer counting times—was necessary to resolve the orthorhombic distortion peaks clearly, resulting in fewer data points being taken. Despite this, it is clear that while there is no systematic variation in the structural transition temperature across

the $Cu_4(OH)_6FX$ series, substitution of the larger halide species predominately at the $2c$ site has a pronounced effect on the nature of the structural transition. A recent study into the structural dynamics of FCl and FBr suggested that the temperature at which the hexagonal to orthorhombic transition begins to occur is related to anisotropic strain, whereby the presence of a larger halide at the $2c$ site expands the lattice anisotropically along the kagomé layer stacking direction. It was proposed that the increased anisotropic strain in FBr compared with FCl would drive the structural transition to higher temperatures.[25] However, here it appears that the converse is true, indicating that additional factors must govern the precise structural transition temperatures across the series, which stem from the synthesis route, or the precise sample composition.

The first step in our analysis of the low-temperature diffraction data was to attempt the refinement of a single *Pnma* phase to each of the I11 datasets taken across the $Cu_4(OH)_6FX$ series. However, in each case, this led to a poor description of the data. For FCl, the addition of a second orthorhombic phase—akin to the two-phase hexagonal model developed to fit the room-temperature data—did not adequately describe the data either. Instead, the best fit to the 90 K data of FCl was obtained with the combination of orthorhombic *Pnma* and hexagonal $P6_3/mmc$ phases with structural parameters and profile parameters allowed to refine independently across the two phases, but U_{iso} values constrained across like-atoms to simplify the fitting procedure. This approach yields $R_{\mathsf{wp}} = 8.13$ %—which is a marked improvement on $R_{\mathsf{wp}} = 13.57$ % for the single-phase *Pnma* model fit—and refined weight fractions of 66.1(2) % and 33.9(2) % for the *Pnma* and $P6_3/mmc$ phases, respectively. Analysis of the HRPD data collected for FCl at 1.5 K using the same two-phase model reveals only a slight increase in the weight fraction of the *Pnma* phase to 68.1(2) %. Final Rietveld fits and results are provided in the Supporting Information.

For the I11 and HRPD data collected on FBr at 90 K and 1.5 K, respectively, a similar

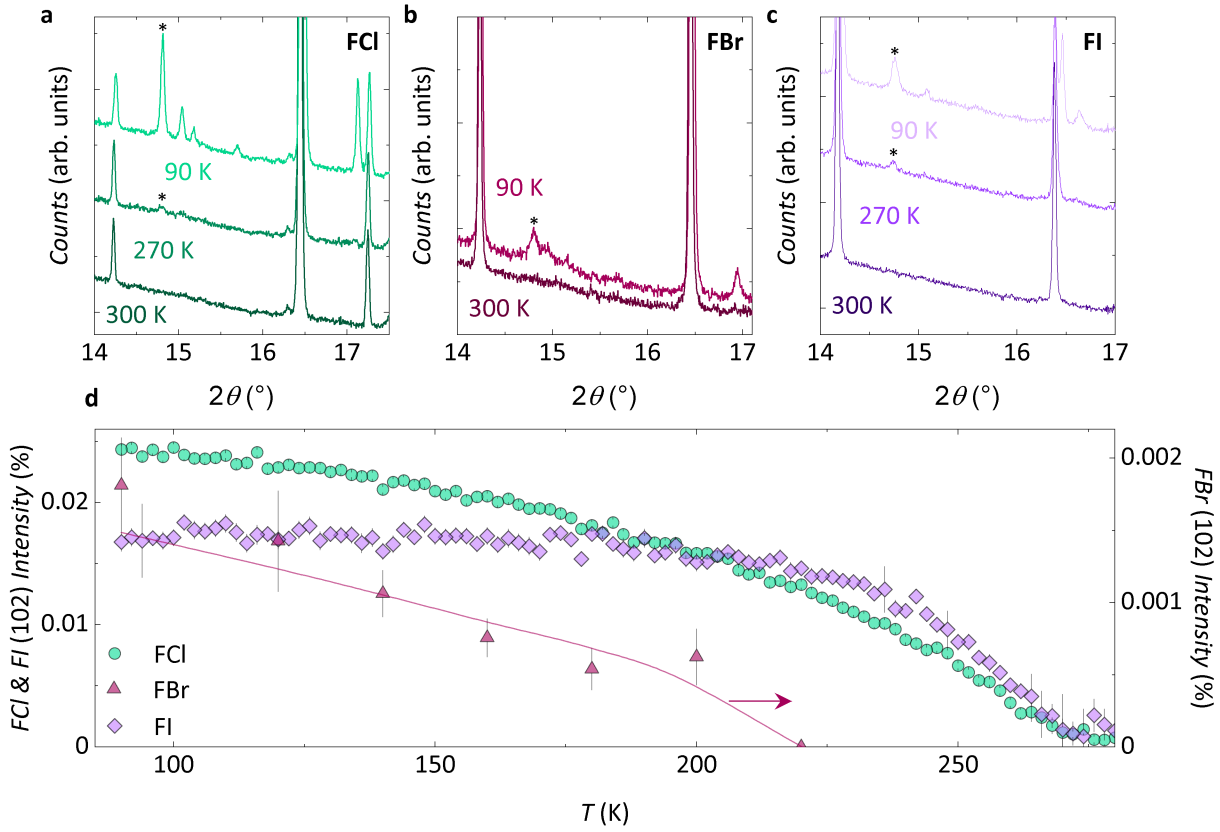

Figure 4: **Elucidating the structural ground state of $Cu_4(OH)_6FX$.** The temperature-dependent high-resolution PXRD data collected on I11 for (a) FCl, (b) FBr and (c) FI. All three samples undergo a structural distortion to an orthorhombic *Pnma* phase, with the most intense orthorhombic distortion peak (102) indicated in each data set by an asterisk. (d) Plotting the (102) peak intensities (as a percentage of the most intense (110) peak) as a function of temperature reveal the dynamics of the structural distortion across the series. The solid line in (d) is a guide to the eye.

two-phase refinement also leads to an improved description of the data with refined weight fractions of 65.0(4) % and 68.8(1) % for the *Pnma* phase at 90 K and 1.5 K, respectively. Conversely, the datasets collected at 90 K and 1.5 K for FI both show two distinct orthorhombic (004) and (602) Bragg peaks, implying that the sample is fully orthorhombic at both temperatures, which is in keeping with the plateau in the orthorhombic peak intensity below 200 K presented for FI in Figure 4. However, the asymmetric peak profile observed in the room-temperature data for FI is still present at low temperatures, but now

for Bragg peaks with $h4\mathsf{n}l$-type reflections as the kagomé layers are stacked along the b-axis in the orthorhombic structure. Thus, below the structural transition at 274 K the data for FI can be modelled using four *Pnma* phases with their F/I ratios fixed to the values determined at 300 K. These fits and refined structures are given in the Supporting Information.

An important result to note here is that at no point in the temperature range measured was it beneficial to use either the *Cmcm* or $P6_3/m$ models reported in the literature and depicted in Fig. 1 to fit the data for any members of the $Cu_4(OH)_6FX$ series. This implies that there is no significant region of temperature in which either of these phases are stable. Instead, it appears that each analogue undergoes a gradual distortion to the orthorhombic *Pnma* phase, but that for FCl and FBr, there is some remaining hexagonal phase at low temperatures. Differences in the *Pnma* model determined here compared to the alternative *Cmcm* and $P6_3/m$ models described in the literature lie predominantly in the ordering scheme of the interlayer Cu3 site. In the *Pnma* structure determined here, the Cu3 ions order cooperatively so that no two move towards each other, whilst in *Cmcm* they shift towards each other in pairs. Meanwhile, in the $P6_3/m$ structure depicted in Fig. 1, both equilateral and scalene triangles emerge within the kagomé planes. As a result, there are also two types of interlayer Cu site, one which is disordered over three sites, as in the room temperature structure, and one which has a site preference. Potential energy surface (PES) calculations for the *Pnma* structure have shown that, of the three possible directions that the distortion can take, the energy barrier is much lower when the interlayer Cu^{2+} shifts in the a direction away from the Cu1 site of the kagomé planes, meaning that there are two energetically equivalent positions shifted towards the Cu2 site. In *Cmcm*, there is a small preference for the Cu3 to shift solely to one site (towards Cu1).[25] Thus, for the *Pnma* structure determined here for the $Cu_4(OH)_6FX$ series, it is not immediately clear why the the Cu^{2+} cations at the interplane site choose one of the two potential directions over the other. However, this observation likely stems from a combination of the sterics involved in this

positional displacement as well as Coulombic forces, making it electrostatically favourable for the interlayer Cu^{2+} ions to shift away from each other with decreasing temperature as the unit cell contracts.

Having determined that all three members of the $Cu_4(OH)_6FX$ series undergo a structural distortion upon cooling, it was clear from our analysis that the Rietveld analysis still did not fully account for the additional orthorhombic peaks observed at low temperatures, especially in terms of their broadness. An example of this effect is shown for FBr in Fig. 5, and we propose that this intrinsic broadening of the orthorhombic peaks indicates residual positional disorder at the Cu^{2+} interplane sites within the low-temperature structures of $Cu_4(OH)_6FX$. Thus, to model this feature in the data, two additional interlayer sites (denoted Cu4 and Cu5) were incorporated into the *Pnma* model and their positions and occupancies were allowed to refine, whilst being constrained so that the sum of the interlayer Cu^{2+} site occupancies (Cu3, Cu4, Cu5) remained equal to one. For FI, the interlayer Cu^{2+} occupancies were additionally constrained to be equal across the four orthorhombic phases. Figure 6 shows the interlayer Cu^{2+}occupancies as a function of temperature for each member of the $Cu_4(OH)_6FX$ series. This analysis shows that for all three analogues there is a preference for the interlayer copper to occupy the Cu3 site—one of the two sites which were shown through PES calculations to be energetically favourable[25] and describe the average *Pnma* structure—but with some remaining Cu^{2+} occupying both of the additional interlayer sites. In FCl, the refined occupancy of Cu3 is 0.950(7) at 90 K and, correspondingly, incorporating this disorder does not significantly improve the Rietveld refinement to I11 data at 90 K compared with a fully ordered model. In addition, it was not possible to refine the Cu4 and Cu5 occupancies in HRPD data collected at 1.5 K, implying that at this temperature the interlayer copper is fully ordered onto the Cu3 site. Conversely, in FBr a model including disorder, leading to Cu4 and Cu5 occupancies of 0.144(5) and 0.146(6) at 90 K, respectively, results in a redistribution of the intensity of the orthorhombic peaks which more closely

matches the collected data, as is clear in the difference profile for this refinement shown in Fig. 5. Even at 1.5 K, there appears to be some remaining interlayer disorder in FBr which contributes to the low intensity of the orthorhombic peaks in the HRPD data at this temperature. Meanwhile, the interlayer copper occupancies appear to plateau in FI below 200 K, in line with the temperature at which the orthorhombic peak intensities plateau, indicating that the structural transition is driven by the order-disorder at the interplane sites. The results of the final Rietveld fit to the low-temperature data of FBr are given in Table 2, with full details of the corresponding refinements of FCl and FI given in the Supporting Information.

Magnetic disorder prevailing in the ground state

Finally, we turn our attention to elucidating the magnetic ground states of each of the members of the $Cu_4(OH)_6FX$ series to explore how the structural complexity induced by competing compositional and positional degrees of freedom affects the magnetic properties that emerge. The magnetic susceptibilities of each sample are presented in Fig. 7a, and each demonstrate a sharp upturn in the susceptibility below 20 K indicating the onset of a magnetic phase transition. These are in accordance with previous magnetometry measurements for FCl and FBr, for which sharp upturns in temperature-dependent magnetic susceptibility data have been reported at $T_{\mathsf{N}} = 17$ K and $T_{\mathsf{N}} = 15$ K, respectively.[21,26,36,37] Curie-Weiss analysis of the high-temperature inverse susceptibility yields negative Weiss constants, θ_{CW}, for each sample, indicating that antiferromagnetic exchange interactions dominate across the series. As shown in Fig. 7b, the magnitude of $|\theta_{\mathsf{CW}}|$ decreases from FCl to FI, likely indicating an increasing contribution of a ferromagnetic component within the magnetic ground states across the series. The effective magnetic moments, μ_{eff}, extracted for the Curie-Weiss fits are also shown in Fig. 7b. These are $\sim$ 10 % larger than the expected spin-only value of $\mu_{\mathsf{eff}} = 3.46\ \mu_{\mathsf{B}}$ per formula unit, but are in line with previously reported values and may

Table 2: Results of the Rietveld refinement of the *Pnma* and $P6_3/mmc$ models of FBr to PXRD and PND data collected on I11 at 90 K and HRPD at 1.5 K, respectively. At 1.5 K, the *Pnma* phase has a weight fraction of 65.0(4) % and $a = 11.5298(2)$ Å, $b = 9.2684(1)$ Å and $c = 6.705031(3)$ Å, while the $P6_3/mmc$ phase has $a = 6.66524(5)$ Å and $c = 9.2629(1)$ Å.

Atom	Site	x	y	z	Occupancy	U_{iso} (Å^2)
			Pnma 90 K			
Cu1	4*a*	0	0	0	1	0.00705(7)
Cu2	8*d*	0.2518(2)	0.5101(1)	0.2496(3)	1	0.00705(7)
Cu3	4*c*	0.1841(3)	0.25	0.0518(5)	0.710(5)	0.00705(7)
Cu4	4*c*	0.186(2)	0.25	0.920(3)	0.144(5)	0.00705(7)
Cu5	4*c*	0.123(2)	0.25	0	0.146(6)	0.00705(7)
F1	4*c*	0.5041(9)	0.25	0.001(2)	1	0.0112(6)
Br1	4*c*	0.3326(2)	0.25	0.5037(3)	1	0.0123(1)
O1	8*d*	0.2986(6)	0.0880(9)	0.011(1)	1	0.0019(3)
O2	8*d*	0.1059(7)	0.0922(8)	0.196(1)	1	0.0019(3)
O3	8*d*	0.4076(6)	0.58877(8)	0.304(1)	1	0.0019(3)
			$P6_3/mmc$ 90 K			
Cu1	6*g*	0.5	0	0	1	0.00705(7)
Cu2	6*h*	0.6283(3)	0.2567(5)	0.25	$\frac{1}{3}$	0.00705(7)
O1	12*k*	0.2016(4)	0.7984(4)	0.9052(6)	1	0.0019(3)
F1	2*b*	0	0	0.75	1	0.0.0123(1)
Br1	2*c*	0.6667	0.3333	0.75	1	0.0123(1)
			Pnma 1.5 K			
Cu1	4*a*	0	0	0	1	0.0051(1)
Cu2	8*d*	0.2493(3)	0.5128(2)	0.2455(4)	1	0.0051(1)
Cu3	4*c*	0.1846(6)	0.25	0.059(1)	0.68(1)	0.0051(1)
Cu4	4*c*	0.189(2)	0.25	0.942(5)	0.19(1)	0.0051(1)
Cu5	4*c*	0.128(3)	0.25	0	0.131(9)	0.0051(1)
F1	4*c*	0.4991(5)	0.25	0.002(1)	1	0.0118(2)
Br1	4*c*	0.3302(3)	0.25	0.5042(8)	1	0.0055(2)
O1	8*d*	0.2971(3)	0.0948(4)	0.0050(7)	1	0.0060(1)
O2	8*d*	0.1044(4)	0.0972(4)	0.1944(6)	1	0.0060(1)
O3	8*d*	0.3996(4)	0.5874(4)	0.3020(6)	1	0.0060(1)
D1	8*d*	0.3755(3)	0.1406(4)	0.0040(8)	1	0.0198(1)
D2	8*d*	0.0608(4)	0.1331(4)	0.3131(6)	1	0.0198(1)
D3	8*d*	0.4374(4)	0.6364(4)	0.1898(6)	1	0.0198(1)
			$P6_3/mmc$ 1.5 K			
Cu1	6*g*	0.5	0	0	1	0.0051(1)
Cu2	6*h*	0.6291(4)	0.2581(9)	0.25	$\frac{1}{3}$	0.0051(1)
O1	12*k*	0.2011(2)	0.7988(2)	0.9103(3)	1	0.0060(1)
D1	12*k*	0.1239(2)	0.8761(2)	0.8693(3)	1	0.0198(1)
F1	2*b*	0	0	0.75	1	0.0118(2)
Br1	2*c*	0.6667	0.3333	0.75	1	0.0055(2)

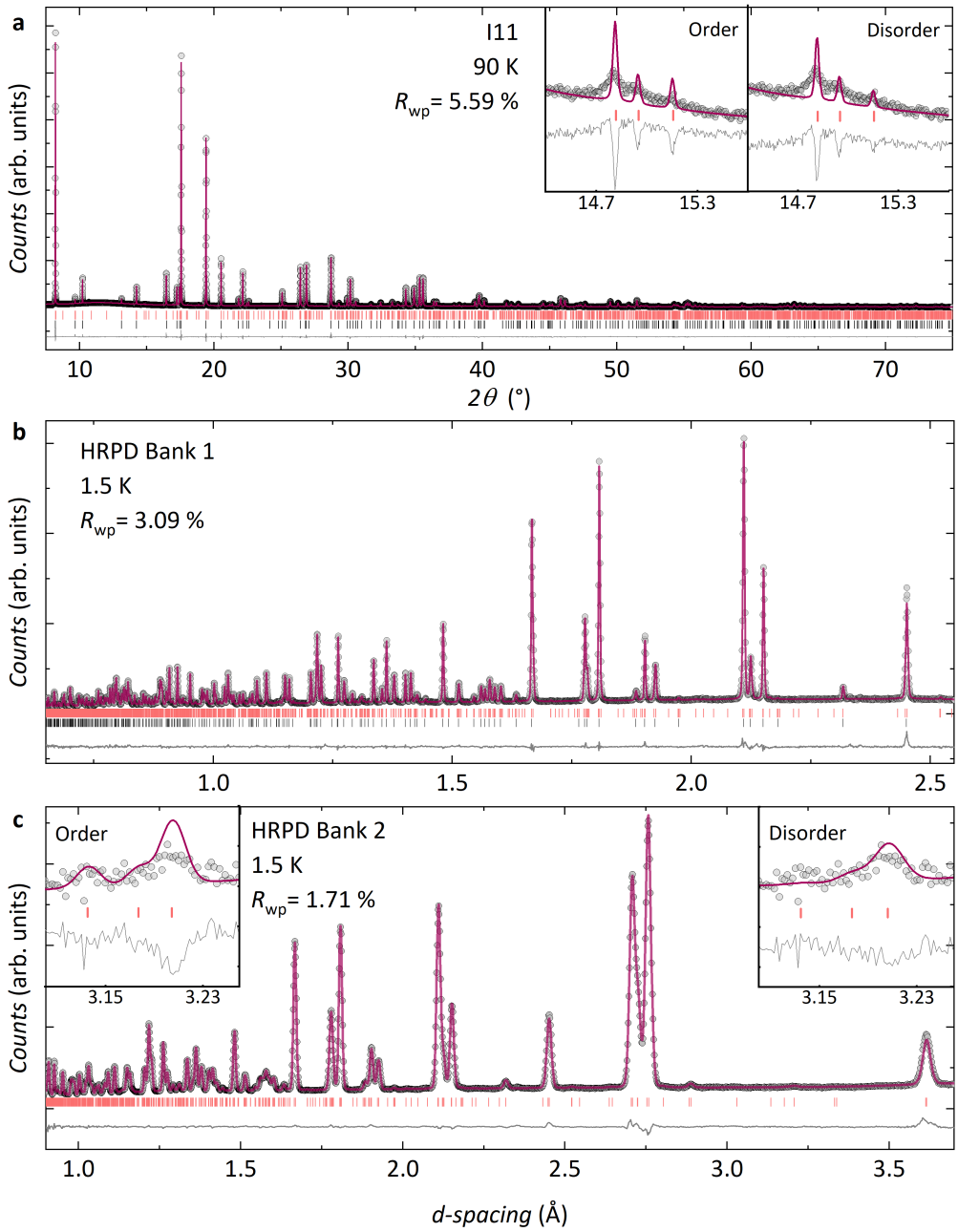

Figure 5: **Persisting disorder in the structural ground state of $Cu_4(OH)_6FX$.** Two-phase Rietveld refinement of *Pnma* (top ticks) and $P6_3/mmc$ (bottom ticks) models to powder diffraction data collected for FBr at (a) 90 K on I11 and 1.5 K on (b) Bank 1 and (b) Bank 2 of HRPD. Insets show the effect of allowing positional disorder at the interplane Cu^{2+} site of the *Pnma* phase.

indicate some orbital contribution to the effective magnetic moment.[19]

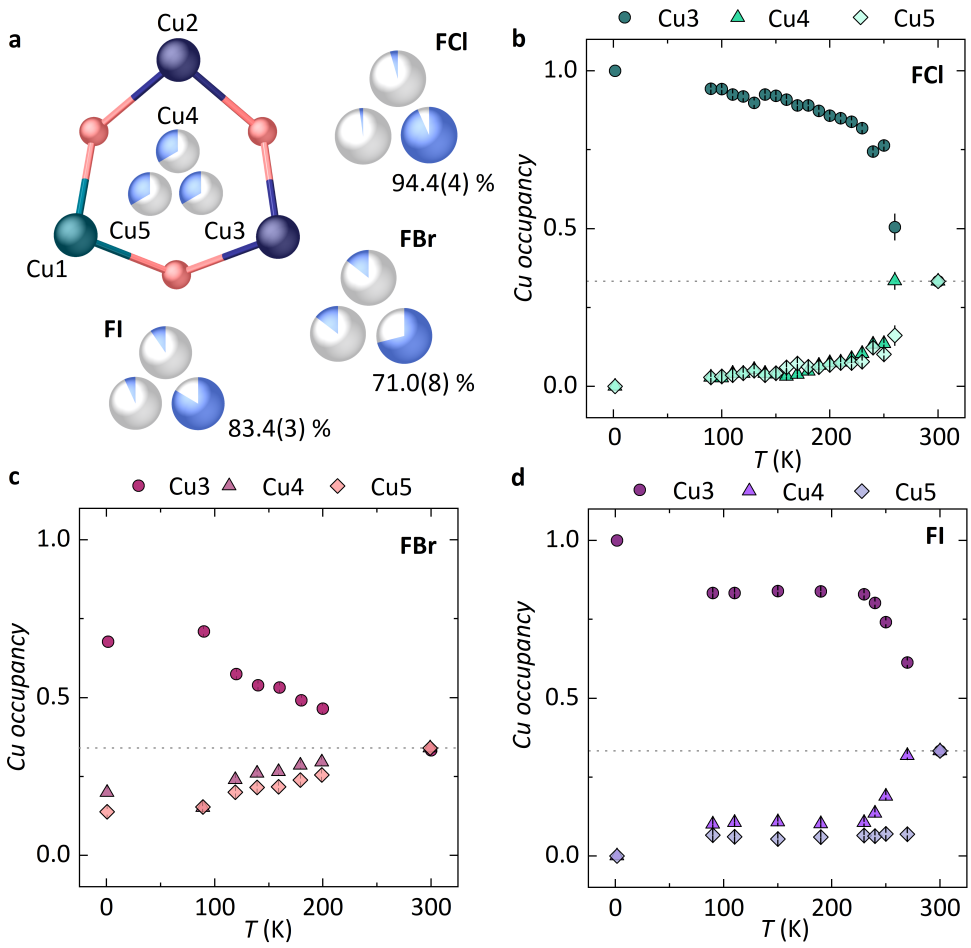

Figure 6: **Positional disorder driving the structural distortion in $Cu_4(OH)_6FX$.** (a) The refined interplane Cu^{2+} occupancies as a function of temperature for the $Cu_4(OH)_6FX$ series at 90 K. The temperature-dependence of these site occupancies for (b) FCl, (c) FBr and (d) FI demonstrate the order-disorder transition driving the hexagonal to orthorhombic structural distortion.

To complement the magnetic susceptibility measurements, heat capacity data collected between $2 - 300$ K for each member of the $Cu_4(OH)_6FX$ series are presented in Fig. 7c. In the absence of suitable non-magnetic analogues, the lattice contribution to the total heat capacity was approximated by fitting $C_{\text{lat}} = \alpha T^2 + \beta T^3$ to the data between $20 - 30$ K, following the approach of several previous studies on barlowite and claringbullite.[19,21,22,24,36] An example of the fitting procedure employed is shown for data collected on FCl in Fig. 7d. Upon subtraction of the estimated lattice contribution, the remaining magnetic heat capac-

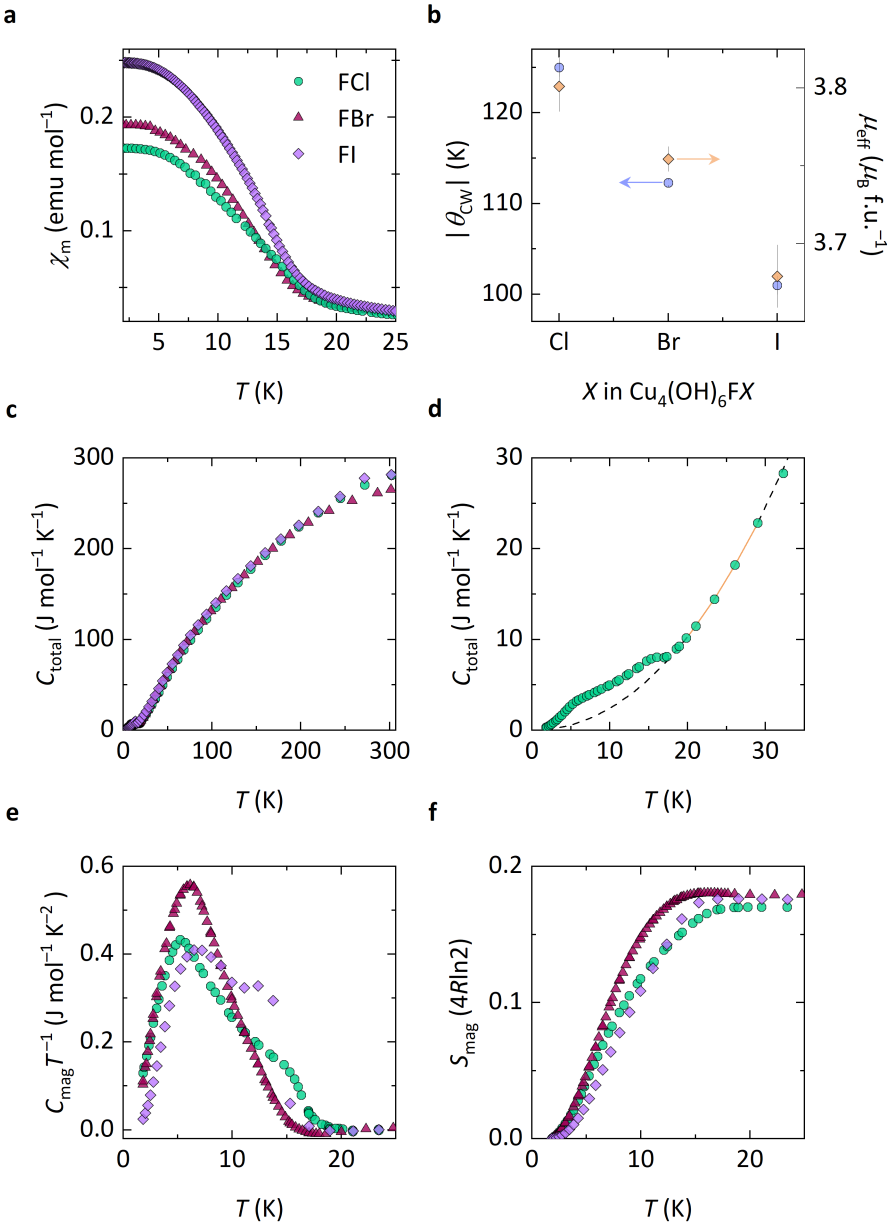

Figure 7: **Magnetic characterisation of Cu$_4$(OH)$_6$FX.** The (a) temperature-dependent magnetic susceptibilities across the series reveal the onset of magnetic order from below 20 K. Curie-Weiss fitting the susceptibility data yields (b) Curie-Weiss constants, θ_{CW}, and effective magnetic moments, μ_{eff}. The (c) total heat capacities of each member of the series have been fit (yellow solid line) to extrapolate (black dashed line) and subtract the lattice contribution. From the resulting (e) magnetic heat capacity, we estimate the (f) magnetic entropy release over the magnetic transitions of Cu$_4$(OH)$_6$FX. Molar magnetic susceptibilities and molar heat capacities have been calculated using the stoichiometric formula mass for each member of the Cu$_4$(OH)$_6$FX series.

ity, C_{mag}, for each system is shown in Fig. 7e. The data demonstrate the presence of broad anomalies below 20 K in all three analogues. In FCl and FI, two anomalies are apparent at 5 K and 15 K (FCl) and 7 K and 13 K (FI), with the less prominent feature in each data set present at higher temperature. In FBr, a single low-temperature broad anomaly is centred at 6 K. The magnetic entropy, S_{mag}, released across the magnetic transitions of each member of the series has been estimated by integrating their respective magnetic heat capacity over $2 - 25$ K and is shown in Fig. 7f. The data show that the entropy released through the magnetic transitions reaches only $\sim$ 18 % of the possible maximum entropy release of $4R\ln 2$ for systems containing four $S = \frac{1}{2}$ moments per formula unit. It has been hypothesised that the recovery of only $\sim$ $\frac{1}{4}$ of the expected entropy in these systems is associated with the ordering of interlayer Cu^{2+} ions[22,24] while the missing entropy has been attributed to the formation of dynamic magnetic moment correlations of the Cu^{2+} ions in the kagomé planes.[19] From our high-flux PND measurements detailed below, however, we know that the magnetic transition below 20 K corresponds to a partial ordering of the magnetic moments on each of the Cu^{2+} ions within the unit cells of each member of the $Cu_4(OH)_6FX$ series. As such, it is likely that the missing magnetic entropy stems from this partial order, implying that the remaining entropy may reside below the 2 K limit of our measurements. The missing entropy may also be hidden in the background subtraction of the data, but note that attempts to fit the background contribution using a Debye model yield the same estimates for the magnetic entropy release[22].

Magnetic heat capacity data revealing two apparent transitions have been reported previously in the literature for both FCl and FBr.[19,22,24,36] Interestingly, the C_{mag} determined here for FBr resembles that of another sample reported in the $P6_3/m$ structure, rather than the $Pnma$ structure presented here. In that case, the gradual incline in C_{mag} was attributed to the short-range ordering of interlayer Cu^{2+} spins.[19,22,24,36] However, this $P6_3/m$ structure is characterised by disorder at the interlayer Cu^{2+} sites, and from our high-resolution

structural study presented above, we now know that there can be residual disorder at the interplane site of the *Pnma* structure of $Cu_4(OH)_6FX$ too, and that this is most pronounced in the FBr analogue. In FCl, the interlayer Cu^{2+} site of the *Pnma* structure is fully ordered, but our high-resolution PXRD data suggests that the FCl sample contains 33.9(2) % of the $P6_3/mmc$ phase, which inherently contains interplane disorder. Meanwhile, FI presents an intermediate degree of positional disorder at this site and PXRD data can be modelled using only orthorhombic phases at low temperature, suggesting that this sample contains the least interplane disorder overall in the series. Therefore, it appears that the higher-temperature transition in C_{mag} is indeed associated with the ordering of interlayer Cu^{2+} moments and that the prominence and temperature of this anomaly correlates with the degree of disorder remaining on these interlayer sites at low temperature across the series. In turn, the discrepancies in the heat capacity data reported in the literature for barlowite, even amongst samples prepared by seemingly similar synthetic routes, may indicate the degree of the disorder at the interlayer site to which the magnetic behaviour appears highly sensitive.

Finally, in order to elucidate the magnetic structure adopted in the ground states of each member we collected high-flux powder neutron diffraction data for each sample within the $Cu_4(OH)_6FX$ series on the D20 diffractometer. In our earlier study of the magnetic structure of the FBr analogue, we established the need for high-flux data collection, as well as the importance of working with temperature-subtracted datasets to resolve the magnetic Bragg peaks of these $S = \frac{1}{2}$ systems.[26] As such, Fig. 8 shows the PND data collected for each sample at 1.5 K after subtraction of a data set collected above 20 K. Initial inspection of the subtracted data reveals that the pattern of magnetic Bragg peaks is largely similar across the series, but with subtle differences in peak intensities. Indeed, refinement of our previously established $Pn'm'a$ magnetic model yields an excellent fit to all datasets, as shown in Fig. 8. Note that, despite the need to include multiple structural phases to model our high-resolution data discussed in the previous two sections, only one magnetic phase is necessary

to model these data due to the relatively low resolution of D20 which, for example, does not capture the peak profile asymmetry of the nuclear Bragg peaks observed in the HRPD data. As such, the results presented here represent an average interpretation of the magnetic structure of each sample.

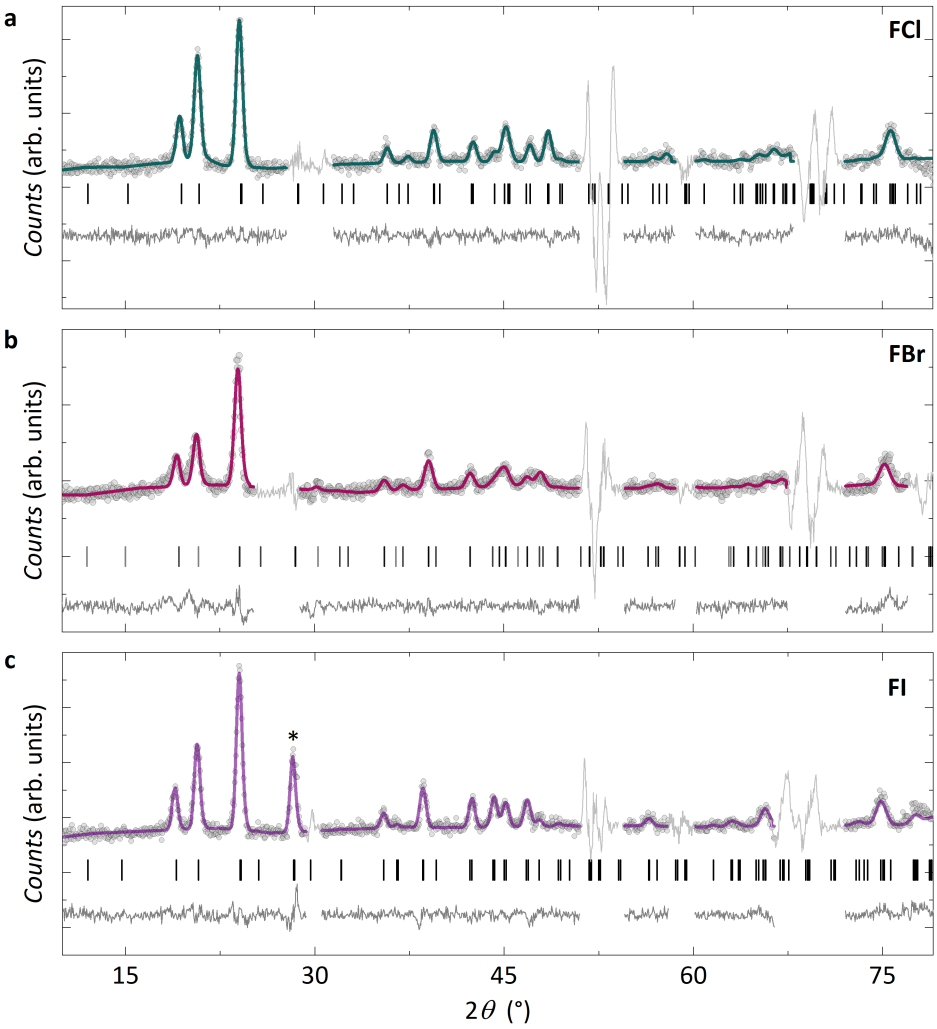

Figure 8: **Elucidating the average magnetic structures of $Cu_4(OH)_6FX$.** Magnetic Rietveld refinements of the $Pn'm'a$ model to subtracted data collected on D20 for (a) FCl, (b) FBr and (c) FI. Light grey regions of the collected data where strong nuclear Bragg peaks exist were excluded from the refinements. The asterisk in (c) marks the (111) reflection.

A representative depiction of the magnetic structure adopted across the $Cu_4(OH)_6FX$ series

is shown for FCl in Fig. 9a. From our analysis, it is clear that the magnetic structures of each analogue can be described by a system of magnetic moments that lie predominantly within the kagomé planes, with an antiferromagnetic canting of the moments on the Cu2 site towards the *b*-axis and a ferromagnetic canting of the moments on the Cu3 site towards the *c*-axis. However, careful comparison of the refined moments shown in Figs. 9b and c, reveals two key differences in the magnetic structures across the series. First, the magnitude of the ordered moments on all three Cu^{2+} sites is significantly larger in FCl and FI than FBr. This suggests that the moment magnitudes are correlated with the remaining interlayer disorder within the *Pnma* structure, which follows from our discussion of the heat capacity data presented in Fig. 7. FCl and FI have a higher degree of interlayer site order, which appears to facilitate longer-range magnetic order and larger ordered moment sizes. Second, while the magnetic ground states of each analogue possess the same pattern of antiferromagnetically and ferromagnetically canted moments, the magnitude of the latter is much larger in FI. This gives rise to the intense (111) magnetic Bragg peak apparent in the diffraction data of FI, which is not resolved for FCl or FBr and stems from the *z*-component of the Cu3 site moment of FI only.

The magnetic structure of FCl at 10 K—in between the two transitions observed within its magnetic heat capacity data—can also be described by the $Pn'm'a$ magnetic model but with reduced moment sizes on each of the Cu^{2+} sites compared to the 1.5 K refinement, as can be seen in Figs. 9b and c. Comparing the refined moments sizes of FCl at 1.5 K and 10 K, it appears that the magnitude of the Cu3 site moment along the *a* axis increases most significantly on cooling to below the 5 K magnetic transition, indicating that it is the ordering of interlayer Cu^{2+} moments that drives this transition. Interestingly, the ordered moment sizes on all sites of each system are substantially reduced from the expected $\mu_{\mathsf{sat}} = 1\ \mu_{\mathsf{B}}$ for $S = \frac{1}{2}$, indicating that strong magnetic frustration prevails in the low-temperature structures of $Cu_4(OH)_6FX$ leading to a partially ordered magnetic ground state. In addition,

analysis of the magnetic Bragg peak profiles also indicates that the extent of the magnetic correlations within the ground state are limited. From the full-width-at-half-maxima of the (001) magnetic Bragg peaks of FCl and FI, magnetic correlation lengths of 149.4(1) Å and 155.4(1) Å can be estimated for each, respectively. For FBr, a broader magnetic Bragg peak profile implies a shorter correlation length of 119.2(1) Å. This is further evidence of the correlation between the degree of positional disorder at the interplane site and the magnetic ground state within the $Cu_4(OH)_6FX$ series, indicating that the greater degree of interplane site disorder remaining in FBr at low temperatures disrupts long-range magnetic order.

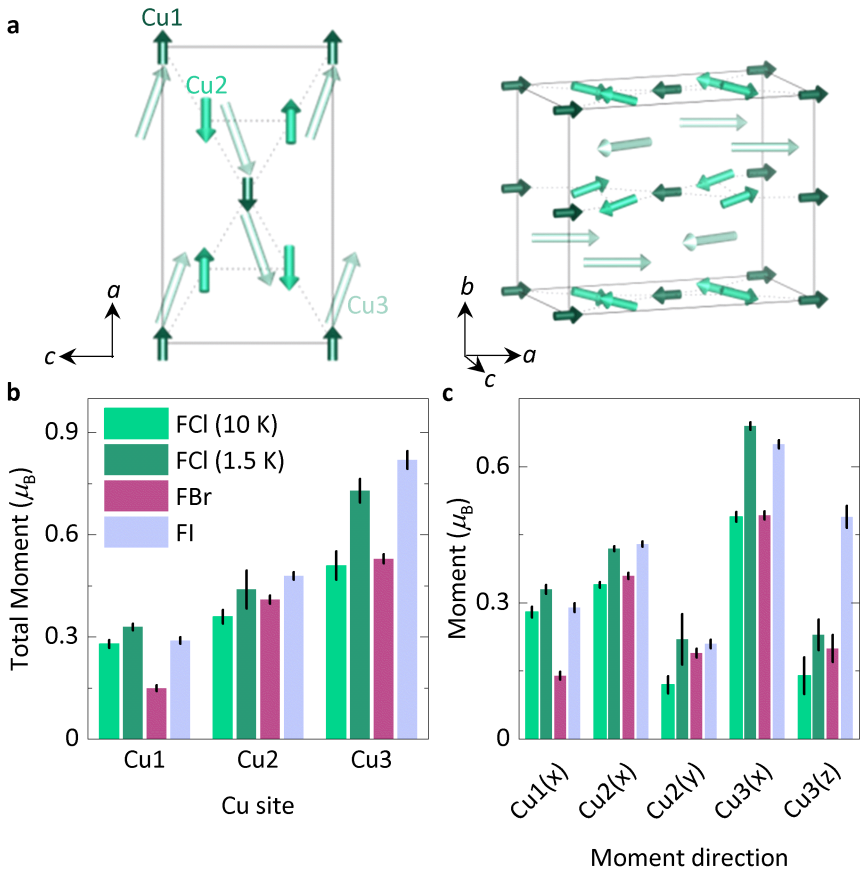

Figure 9: **Comparing the magnetic ground states across $Cu_4(OH)_6FX$.** (a) A representative visualisation of the $Pn'm'a$ magnetic structure adopted across the series at low-temperatures. In this case, the magnetic structure for FCl is shown. While the average magnetic structure is maintained across the series, the (b) and (c) moment sizes vary and correlate with the degree of positional disorder at the interplane Cu^{2+} site.

Conclusions & Outlook

In summary, this work provides a comprehensive investigation of the synthesis, crystal and magnetic structures of the barlowite family of $S = \frac{1}{2}$ kagomé magnets, revealing the complex interplay between structural and magnetic (dis)orders within these systems. Barlowite, $Cu_4(OH)_6FBr$, claringbullite, $Cu_4(OH)_6FCl$, and their novel iodide analogue, $Cu_4(OH)_6FI$, each adopt a structure containing kagomé layers of Cu^{2+} ions, which at room temperature can be described using a hexagonal $P6_3/mmc$ model. Upon cooling, each member of the series undergoes a structural distortion driven by the partial ordering of Cu^{2+} ions at the interplane site. The crystal structures of the samples reported here are best described below the transition by an orthorhombic $Pnma$ model, however, the high-resolution powder X-ray and neutron diffraction data presented here have revealed residual disorder at the interplane site of this orthorhombic model. Indeed, a key conclusion of this work is that there are two distinct sources of structural complexity within the family of materials, as summarised in Table 3. First, across the series there is evidence for the presence of multiple compositional phases within powder samples, giving rise to a systematic peak profile asymmetry in high-resolution powder diffraction data that can be ascribed to compositional disorder of the halide species between the kagomé layers. This is particularly pronounced for FI, and so may be driven by the anisotropic strain imposed on the lattice by the larger ionic radius of the iodide anions in comparison to its chloride and bromide analogues. Second, while the presence of positional disorder of the Cu^{2+} ions at the interplane site of the hexagonal room-temperature structure of this series was previously well-established, refinement of interlayer Cu^{2+} occupancies within the low-temperature $Pnma$ phase demonstrates that such positional disorder remains on the interlayer site at 1.5 K, particularly in FBr. This leads to another important conclusion of this work, which is that understanding this structural disorder is key, as it is highly correlated to the magnetic ground state properties of the $Cu_4(OH)_6FX$ series. Both magnetic heat capacity data and high-flux powder neutron diffraction measurements reveal that the extent of long-range magnetic order is governed by

the degree of interlayer Cu^{2+} disorder prevailing in the structural ground state. The average magnetic structures of the $Cu_4(OH)_6FX$ series are well described by the $Pn'm'a$ magnetic space group, but with ordered moment sizes and magnetic correlation lengths inversely proportional to the degree of positional disorder at the interplane site. Across the series, the reduced ordered moment sizes are evidence of only partial magnetic order in the ground state.

Table 3: The degree of compositional disorder between the halide ions between the kagomé layers of $Cu_4(OH)_6FX$ is most pronounced for the system with the largest halide species, FI. However, the residual positional disorder at the interplane Cu^{2+} site in the low-temperature orthorhombic structure is most pronounced for FBr. The positional disorder correlates most strongly with the degree of partial magnetic order observed at low temperatures.

Disorder Induced Complexity in $Cu_4(OH)_6FX$	
Degree of compositional disorder	FI > FBr ≈ FCl
Degree of positional disorder	FBr > FCl > FI
Degree of magnetic disorder	FBr > FCl > FI

The various forms of disorder reported here—as well as the competing structural phases reported in the literature for members of the $Cu_4(OH)_6FX$ series—are important reminders of the need for careful control and reporting of synthetic conditions in future studies of these compounds. Sample dependence and its strong correlation to magnetic ground state properties is an increasingly prevalent theme in the study of frustrated quantum magnets[38], and future work on the barlowite family of $S = \frac{1}{2}$ kagomé magnets should aim to gain an understanding of how the various reported structures and structural defects form *in situ*. The diffraction-based study presented here provides a comprehensive understanding of the average crystal and magnetic structures within this family of materials. However, this study also represents the limit of what we can understand of the fascinating and complex structure-property relationships within the $Cu_4(OH)_6FX$ series from this average-structure perspective. Whilst there will undoubtedly be value in further single-crystal diffraction

studies of barlowite and its analogues, future studies should also make use of local structure techniques, such as NMR spectroscopy and total scattering, to gain clearer insight into the compositional and positional disorders present within these systems. Combining this with experiments that will capture the details of the partial disorder present within the magnetic ground states of $Cu_4(OH)_6FX$ alluded to through the high-flux neutron diffraction data present here—in particular, inelastic and diffuse neutron scattering measurements—will ultimately yield a deeper understanding of the relationship between structural and magnetic (dis)orders in this family of materials. Finally, we hope that this study also serves as motivation for further computational studies of the $Cu_4(OH)_6FX$ series to determine the relative stability of the various proposed structures of barlowite and its halide analogues, and how the magnetic exchange pathways vary across the series.

Acknowledgement

The authors thank the University of Liverpool for provision of a PhD studentship to K. Tustain and the STFC for access to beam time at the Diamond Light Source (instrument ID11, proposal CY24154), ISIS Neutron and Muon Source and the Institut Laue-Langevin. The authors also thank A. H. Abdeldaim and J. N. Graham (University of Birmingham) for assistance with beam time measurements, Dr H. Niu (University of Liverpool) for assistance with magnetometry measurements and Dr S. J. Cassidy (University of Oxford) for helpful discussions regarding modelling powder diffraction data.

Supporting Information Available

Full details of Rietveld analysis of X-ray and neutron data are provided online. Neutron diffraction data can be accessed at DOI:10.5286/ISIS.E.RB1910099 (HRPD, ISIS), DOI:10.5291/ILL-DATA.5-31-2632 (D20, ILL).

References

(1) Norman, M. R. Colloquium: Herbertsmithite and the search for the quantum spin liquid. *Rev. Mod. Phys.* **2016**, *88*, 041002.

(2) Senn, M. S.; Wright, J. P.; Attfield, J. P. Charge order and three-site distortions in the Verwey structure of magnetite. *Nature* **2012**, *481*, 173–176.

(3) Chamorro, J. R.; McQueen, T. M.; Tran, T. T. Chemistry of Quantum Spin Liquids. *Chem. Rev.* **2021**, *121*, 2898–2934.

(4) Broholm, C.; Cava, R. J.; Kivelson, S. A.; Nocera, D. G.; Norman, M. R.; Senthil, T. Quantum spin liquids. *Science* **2020**, *367*.

(5) Basov, D. N.; Averitt, R. D.; Hsieh, D. Towards properties on demand in quantum materials. *Nat. Phys.* **2017**, *16*, 1077–1088.

(6) Han, T.-H.; Helton, J. S.; Chu, S.; Nocera, D. G.; Rodriguez-Rivera, J. A.; Broholm, C.; Lee, Y. S. Fractionalized excitations in the spin-liquid state of a kagome-lattice antiferromagnet. **2012**, *492*, 406–410.

(7) Fu, M.; Imai, T.; Han, T.-H.; Lee, Y. S. Evidence for a gapped spin-liquid ground state in a kagome Heisenberg antiferromagnet. *Science* **2015**, *350*, 655–658.

(8) Khuntia, P.; Velazquez, M.; Barthélemy, Q.; Bert, F.; Kermarrec, E.; Legros, A.; Bernu, B.; Messio, L.; Zorko, A.; Mendels, P. Gapless ground state in the archetypal quantum kagome antiferromagnet $ZnCu_3(OH)_6Cl_2$. *Nat. Phys.* **2020**, *16*, 469–474.

(9) Wang, J.; Yuan, W.; Singer, P. M.; Smaha, R. W.; He, W.; J, W.; Lee, Y. S.; Imai, T. Emergence of spin singlets with inhomogeneous gaps in the kagome lattice Heisenberg antiferromagnets Zn-barlowite and herbertsmithite. *Nat. Phys.* **2021**, *17*, 1109—-1113.

(10) Malcherek, T.; Welch, M. D.; Williams, P. A. The atacamite family of minerals – a testbed for quantum spin liquids. *Acta Cryst. B* **2018**, *74*, 519–526.

(11) Zheng, X. G.; Kawae, T.; Kashitani, Y.; Li, C. S.; Tateiwa, N.; Takeda, K.; Yamada, H.; Xu, C. N.; Ren, Y. Unconventional magnetic transitions in the mineral clinoatacamite $Cu_2Cl(OH)_3$. *Phys. Rev. B* **2005**, *71*, 052409.

(12) Wills, A. S.; Henry, J.-Y. On the crystal and magnetic ordering structures of clinoatacamite, γ-$Cu_2(OD)_3Cl$, a proposed valence bond solid. *J. Phys.: Condens. Matter* **2008**, *20*, 472206.

(13) Zenmyo, K.; Kubo, H.; Tokita, M.; Hamasaki, T.; Hagihala, M.; Zheng, X. G.; Kawae, T.; Takeuchi, Y.; Matsumura, M. Proton NMR study of atacamite $Cu_2Cl(OH)_3$. *J. Phys. Soc. Japan* **2013**, *82*.

(14) Braithwaite, R. S. W.; Mereiter, K.; Paar, W. H.; Clark, A. M. Herbertsmithite, $Cu_3Zn(OH)_6Cl_2$, a new species, and the definition of paratacamite. *Mineral. Mag.* **2004**, *68*, 527–539.

(15) Freedman, D. E.; Han, T. H.; Prodi, A.; Müller, P.; Huang, Q. Z.; Chen, Y. S.; Webb, S. M.; Lee, Y. S.; McQueen, T. M.; Nocera, D. G. Site specific X-ray anomalous dispersion of the geometrically frustrated kagomé magnet, herbertsmithite, $ZnCu_3(OH)_6Cl_2$. *J. Am. Chem. Soc.* **2010**, *132*, 16185–16190.

(16) Nilsen, G. J.; De Vries, M. A.; Stewart, J. R.; Harrison, A.; Rønnow, H. M. Low-energy spin dynamics of the $S = \frac{1}{2}$ kagome system herbertsmithite. *J. of Phys.: Condens. Matter* **2013**, *25*, 106001.

(17) Han, T. H.; Isaacs, E. D.; Schlueter, J. A.; Singleton, J. Anisotropy: Spin order and magnetization of single-crystalline $Cu_4(OH)_6FBr$ barlowite. *Phys. Rev. B* **2016**, *93*, 214416.

(18) Elliott, P.; Cooper, M. A.; Pring, A. Barlowite, $Cu_4FBr(OH)_6$, a new mineral isotructural with claringbullite: description and crystal structure. *Mineral. Mag.* **2014**, *78*, 1755–1762.

(19) Han, T. H.; Singleton, J.; Schlueter, J. A. Barlowite: A spin-$\frac{1}{2}$ antiferromagnet with a geometrically perfect kagome motif. *Phys. Rev. Lett.* **2014**, *113*, 227203.

(20) Jeschke, H. O.; Salvat-Pujol, F.; Gati, E.; Hoang, N. H.; Wolf, B.; Lang, M.; Schlueter, J. A.; Valentí, R. Barlowite as a canted antiferromagnet: Theory and experiment. *Phys. Rev. B* **2015**, *92*, 094417.

(21) Feng, Z.; Wei, Y.; Liu, R.; Yan, D.; Wang, Y. C.; Luo, J.; Senyshyn, A.; Cruz, C. D.; Yi, W.; Mei, J. W.; Meng, Z. Y.; Shi, Y.; Li, S. Effect of Zn doping on the antiferromagnetism in kagome $Cu_{4-x}Zn_x(OH)_6FBr$. *Phys. Rev. B* **2018**, *98*, 155127.

(22) Pasco, C. M.; Trump, B. A.; Tran, T. T.; Kelly, Z. A.; Hoffmann, C.; Heinmaa, I.; Stern, R.; Mcqueen, T. M. Single-crystal growth of $Cu_4(OH)_6BrF$ and universal behavior in quantum spin liquid candidates synthetic barlowite and herbertsmithite. *Phys. Rev. Mater.* **2018**, *2*, 44406.

(23) Ranjith, K. M.; Klein, C.; Tsirlin, A. A.; Rosner, H.; Krellner, C.; Baenitz, . M. Magnetic resonance as a local probe for kagome magnetism in Barlowite $Cu_4(OH)_6FBr$. *Sci. Rep.* **2018**, *8*, 10851.

(24) Smaha, R. W.; He, W.; Sheckelton, J. P.; Wen, J.; Lee, Y. S. Synthesis-dependent properties of barlowite and Zn-substituted barlowite. *J. Solid State Chem.* **2018**, *268*, 123–129.

(25) Henderson, A.; Dong, L.; Biswas, S.; Revell, H. I.; Xin, Y.; Valentí, R.; Schlueter, J. A.; Siegrist, T. Order-disorder transition in the $S = \frac{1}{2}$ kagome antiferromagnets claringbullite and barlowite. *Chem. Commun.* **2019**, *55*, 11587–11590.

(26) Tustain, K.; Nilsen, G. J.; Ritter, C.; da Silva, I.; Clark, L. Nuclear and magnetic structures of the frustrated quantum antiferromagnet barlowite, $Cu_4(OH)_6FBr$. *Phys. Rev. Mater.* **2018**, *2*, 111405.

(27) Guterding, D.; Valentí, R.; Jeschke, H. O. Reduction of magnetic interlayer coupling in barlowite through isoelectronic substitution. *Phys. Rev. B* **2016**, *94*, 125136.

(28) Liu, Z.; Zou, X.; Mei, J.-W.; Liu, F. Selectively doping barlowite for quantum spin liquid: A first-principles study. *Phys. Rev. B* **2015**, *92*, 220102.

(29) Tustain, K.; Ward-O'Brien, B.; Bert, F.; Han, T.-H.; Luetkens, H.; Lancaster, T.; Huddart, B. M.; Baker, P. J.; Clark, L. From magnetic order to quantum disorder in the Zn-barlowite series of $S = \frac{1}{2}$ kagomé antiferromagnets. *npj Quantum Materials* **2020**, *5*, 74.

(30) Smaha, R. W. et al. Materializing rival ground states in the barlowite family of kagome magnets: quantum spin liquid, spin ordered, and valence bond crystal states. *npj Quantum Materials* **2020**, *5*, 1.

(31) Fejer, E. E.; Clark, A. M.; Couper, A. G.; Elliott, C. J. Claringbullite, a new hydrated copper chloride. *Mineral. Mag.* **1977**, *41*, 433–436.

(32) Burns, P. C.; Cooper, M. A.; Hawthorne, F. C. Claringbullite; a Cu^{2+} oxysalt with Cu^{2+} in trigonal-prismatic coordination. *Can. Min.* **1995**, *33*, 633–639.

(33) David, W. I. F.; Jones, M. O.; Gregory, D. H.; Jewell, C. M.; Johnson, S. R.; Walton, A.; Edwards, P. P. A Mechanism for Non-stoichiometry in the Lithium Amide/Lithium Imide Hydrogen Storage Reaction. *J. Am. Chem. Soc.* **2007**, *129*, 1594–1601.

(34) Nytko, E. A. Synthesis, structure, and magnetic properties of $S = \frac{1}{2}$ kagomé antiferromagnets. Ph.D. thesis, Massachusetts Institute of Technology, 2008.

(35) Welch, M. D.; Najorka, J.; Rumsey, M. S.; Spratt, J. The hexagonal to orthorhombic structural phase transition in claringbullite, $Cu_4FCl(OH)_6$. *Can. Min.* **2021**, *59*, 265–285.

(36) Yue, X. Y.; Ouyang, Z. W.; Wang, J. F.; Wang, Z. X.; Xia, Z. C.; He, Z. Z. Magnetization and ESR studies on $Cu_4(OH)_6FCl$: An antiferromagnet with a kagome lattice. *Phys. Rev. B* **2018**, *97*, 54417.

(37) Feng, Z.; Yi, W.; Zhu, K.; Wei, Y.; Miao, S.; Ma, J.; Luo, J.; Li, S.; Yang Meng, Z.; Shi, Y. From claringbullite to a new spin liquid candidate $Cu_3Zn(OH)_6FCl$. *Chin. Phys. Lett.* **2019**, *36*, 017502.

(38) Bowman, D. F.; Cemal, E.; Lehner, T.; Wildes, A. R.; Mangin-Thro, L.; Nilsen, G. J.; Gutmann, M. J.; Voneshen, D. J.; Prabhakaran, D.; Boothroyd, A. T.; Porter, D. G.; Castelnovo, C.; Refson, K.; Goff, J. P. Role of defects in determining the magnetic ground state of ytterbium titanate. *Nat. Comms.* **2019**, *10*, 637.